Nanostructured intermetallic InSb as a high-capacity and high-performance negative electrode for sodium-ion batteries

Irshad Mohammad, Lucie Blondeau, Eddy Foy, Jocelyne Leroy, Eric Leroy, Hicham Khodja, Magali Gauthier

Nanostructured intermetallic InSb as a high-capacity and high-performance negative electrode for sodium-ion batteries

Irshad Mohammad[*†], *Lucie Blondeau*[†], *Eddy Foy*[§], *Jocelyne Leroy*[‡], *Eric Leroy*[⊥], *Hicham Khodja*[†], *Magali Gauthier*[*†]

[†] Université Paris-Saclay, CEA, CNRS, NIMBE, LEEL, 91191, Gif-sur-Yvette, France

[§] Université Paris-Saclay, CEA, CNRS, NIMBE, LAPA-IRAMAT, 91191 Gif-sur-Yvette, France

[‡] Université Paris-Saclay, CEA, CNRS, NIMBE, LICSEN, 91191 Gif-sur-Yvette, France

[⊥] Université Paris Est Créteil, CNRS, ICMPE, UMR 7182, 2 rue Henri Dunant, 94320 Thiais, France

KEYWORDS: antimony, indium, intermetallic compound, nanostructured, negative electrode, sodium-ion batteries

ABSTRACT. Following the trends of alloys as negative electrodes for Na-ion batteries, the sodiation of the nanostructured InSb intermetallic compound was investigated. The benefit of coupling Sb with In was evaluated through the synthesis of InSb by a chemical reduction in the form of nanostructured particles assembled in micrometric aggregates. After a full structural, morphological and surface characterization, the electrochemical performance of nanostructured InSb was examined in a carbonated electrolyte with fluoroethylene carbonate (FEC) as additive. The performance turns out to be remarkable with a capacity around 450 mAh g^{-1} after 50 cycles

at C/5. In terms of cyclability, the capacity of InSb is impressively stable at 1C with a capacity retention of 96 % up to 100 cycles, in contrast to the strong capacity decay observed for a nanostructured Sb electrode. A good high-rate behavior is also observed with a capacity of 310 mAh g^{-1} at 5C. The better stability of the InSb compound compared to pure Sb suggests that combining In with Sb improves the ability of the material to alleviate volume expansion and mechanical stress during the repeated sodiation/desodiation processes. X-Ray photoelectron spectroscopy and electrochemical impedance spectroscopy on cycled electrodes were finally implemented to shed light respectively on the surface chemistry and electrochemical stability behavior of the promising InSb compound.

INTRODUCTION

Currently, lithium-ion batteries (LIBs) provide portable electricity to electronic gadgets such as mobile phones, laptops and tablets, and are used to supply energy to medical equipment, electric vehicles and power tools.[1] While LIBs are the dominate power source for various electronic applications, some issues remain such as high lithium cost and limited availability of Li, Co and Ni.[2,3] Today, the research of alternative technologies, i.e. beyond-Li-ion batteries is highly motivated by an increasing need of efficient energy storage systems for portable electronic equipment, electric vehicles, and large-scale smart grids.

To end this, several post-lithium battery systems based on Na^+, Mg^{2+}, Al^{3+}, Ca^{2+}, K^+, F^-, Cl^- charge carriers have been introduced and are actively investigated.[4–15] Among all, sodium-ion batteries (NIBs) attracted attention as a strong alternative to LIBs for mainly large-scale energy storage due to the low cost and large abundance of sodium, and its uniform presence around the globe.[5,16–18] Since sodium belongs to the same group of the periodic table as lithium, it possesses similar physical and chemical properties in addition to a low redox potential of -2.71 V (vs. SHE). However, the atomic size of sodium ion (1.02 Å) is larger than that of lithium ion (0.76

Å), which leads to differences in electrochemistry.[19] The initial development of NIBs was adapted from well-known lithium-ion systems, consequently several well-developed LIB positive electrodes were directly utilized for NIBs.[20–22] Unlike some positive electrodes, the usage of graphite as negative electrode for NIBs is quite limited due to the large size of sodium ions[23–25] Therefore, it is necessary to find other negative electrodes with high capacity and excellent cycling for NIBs. The negative electrode materials for sodium storage are mainly classified into four types: intercalation reaction-based materials,[26,27] conversion reaction-based materials,[28,29] carbonaceous materials,[30,31] and alloying materials.[32] Among them, alloy-type negative materials show great expectations due to their remarkable theoretical capacities. For example, Si, Ge, Sn, and Pb alloys show theoretical capacities of 954, 369, 847, and 485 mAh g^{-1}, respectively.[6] However, practical application of these alloys is restricted by their large volume expansion during sodiation and desodiation processes (see Table S1, Supplementary Information). Sb alloy is considered as one of the best negative electrodes for NIBs.[33] Sb can combine with sodium to form a binary compound with composition of Na_3Sb, exhibiting a theoretical capacity of 660 mAh g^{-1}. Despite such high capacity and a relatively stable voltage (0.4 vs Na/Na^+), practical implementation of Sb anode for NIBs is held back by the severe volumetric expansion (300%) during cycling.[34,35] Volume change leads to physical disconnection of active material from electronic additives and binder, which eventually leads to rapid capacity fading.

To address the volume change issue, several efforts are made to design new structures favorable for alleviating volumetric stress and ensuring a high ionically and electronically conductive environment. One strategy is to control the particle size, e.g. by preparing nanosized Sb particles by ball-milling or chemical synthesis route, dispersing Sb nanoparticles in carbon matrix, and depositing Sb particles on conductive film.[36–38] A second approach involves the design of nanostructured electrodes such as yolk-shell Sb@C structures,[39] nanoporous structures

(mesoporous Sb_2O_3@Sb nanocomposite),[40] and self-supported nanostructures[41] that are able to overcome the volume change, and hence to improve the electrochemical performance of NIBs. Another effective strategy is to design intermetallic Sb_x-M_y alloys. In contrast to pure metal, intermetallic compounds have shown superior cycling performance in NIBs. Indeed, they can serve as a buffer matrix that can relax the volume variation of active Sb during alloying/dealloying process and thus enhance the electrochemical performance. Already some intermetallic alloys such as SnSb, Sb_2Te_3, Bi–Sb, and Si-Sb have been prepared and investigated as anode material for NIBs.[42–45] A SnSb/C composite electrode exhibited a first charge capacity of 544 mAh g^{-1} at current density of 100 mA g^{-1}, while 80 % of the capacity could be recovered after 50 cycles.[42] BiSb-C electrode delivered an initial charge capacity of 375 mAh g^{-1} with a capacity retention of 78% after 50 cycles.[44] In earlier reports, InSb alloys have been investigated as a promising anode material for LIBs,[46] and magnesium-ion batteries (MIBs).[47] Very recently, Usui et al.[48] demonstrated the capability of the InSb alloy as anode host for sodium storage and compared its performance with other metallic analogues (Sb_2Se_3, $FeSb_2$, LaSb, and SnSb). InSb synthesized via a mechanochemical route shows a reversible capacity of 415 mAh g^{-1} at 30°C in an ionic liquid based electrolyte until the 250th cycle at a current density of 50 mA g^{-1}, before a sudden capacity fading is observed. Yet, the rate performance was not evaluated, while some questions remain on the reaction mechanisms and reactivity of InSb at the electrode/electrolyte interface.

In the present study, we are pushing the performance and understanding of Na storage in the InSb intermetallic compound through nanostructuration. We have synthesized nanostructured InSb alloy via a simple chemical reduction route and demonstrated its remarkable cycling performance as a negative electrode for high performance sodium-ion batteries, competing with ball-milled InSb[48] and with the best Sb electrodes in literature. Further, the cycling performance of the nanostructured InSb anode is compared to that of nanostructured Sb anode (synthesized

via the same chemical reduction) for NIBs. The InSb nanostructured compound shows better cycling performance as compared to the Sb electrode. The chemical composition of the InSb electrode surface was analyzed by X-ray photoelectron spectroscopy (XPS). To gain further insight on the sodiation/desodiation reaction mechanisms, *ex situ* X-ray diffraction (XRD) measurement was performed. Finally, *operando* XRD was used to give a glimpse of the sodiation mechanism in real time condition.

EXPERIMENTAL METHODS

Material Preparation

Chemical reduction in a solution was used to synthesize nanostructured InSb and Sb particles, according to a previous report.[49] A detailed schematic of the reduction process for the synthesis of the active material is given in Figure S1. In this synthesis, the chlorinated precursors are first dissolved and reduced using metallic zinc. For the synthesis of InSb, the $InCl_3$ (Alfa Aesar, 99.999 %) and $SbCl_3$ (Sigma-Aldrich, 99.99 %) precursors were first dissolved in 15 mL of deaerated ethylene glycol (Sigma-Aldrich,> 99.9 %) under an Ar inert atmosphere (in a glove box). Then metallic zinc (Alfa Aesar, 99.9 %) was added to the solution, which was stirred magnetically for 24 h. The resulting solution was filtered and washed several times with methanol to remove $ZnCl_2$. The as-filtered powder was dried at 110 °C for 2 h prior to annealing in a tube furnace in an airtight stainless-steel container at 400 °C for 4 h under argon. The Sb particles were synthesized in a similar fashion as of InSb, with a $SbCl_3$ precursor.

Preparation of electrodes and electrochemical characterization

Active materials (InSb or Sb), conductive carbon black (Super P), and CMC (binder) were mixed in water at a ratio of 70:20:10 wt%. The mixture was stirred using a milling apparatus (MM400, Retsch) for 20 minutes, forming a homogenous slurry. Subsequently, the slurry was uniformly deposited on Cu foils (12 µm, Oak Mitsui) using a spiral film applicator and then dried at room temperature for 12 h. The electrodes were punched into discs (14 mm in diameter)

with a mean mass loading of 0.65 ± 0.13 mg/cm^2 and dried at 110 °C for 24 h under vacuum prior to storage in the glove box. A Na foil (Sigma-Aldrich, 99.99 %) was used as counter and reference electrodes and glass fibres (GF/A, Whatman) served as separator. A 1 M $NaClO_4$ in ethylene carbonate (EC) and dimethyl carbonate (DMC) (1:1) with 5 wt % addition of fluoroethylene carbonate (FEC) was selected as the electrolyte. Swagelok cells were assembled in an argon filled glovebox and subsequently rested for 5 h before electrochemical cycling. The electrochemical charge-discharge profiles were assessed with a VMP3 Biologic potentiostat in galvanostatic mode between 0.05 and 2 V (versus Na^+/Na). Cyclic voltammetry (CV) experiments were performed at scan rates between 0.1 and 5 mV s^{-1} between 0.01 and 2.0 V (versus Na^+/Na). Electrochemical impedance spectroscopy (EIS) measurements were performed in the frequency range of 1 MHz to 1 Hz and with a voltage amplitude of 5 mV. For operando XRD measurement, electrodes were prepared by mixing and pressing 70 wt % of active material, 10 wt % of carbon black and 20 wt % of polytetrafluoroethylene (PTFE) together in an agate mortar. A home-made electrochemical cell based on a Be window was used for XRD acquisition in reflection mode. For XPS analysis, the electrodes were recovered after disassembling the cells and washed gently with pure dimethyl carbonate (DMC).

Surface and Structural Characterization

Structures of the as-prepared powders were characterized by XRD on a RU-200B rotating anode X-ray generator equipped with Mo $K\alpha_{1,2}$ radiation (λ=0.7093 Å). Spherical diffraction patterns were acquired using a Pilatus 300K hybrid pixel detector (Dectris). The software FIT2D[50] was used to integrate the diffraction patterns. Scanning Electron Microscopy (SEM) was employed with a SEM-FEG Zeiss Ultra 55 model operating at 3kV to probe the surface morphology of the samples. Transmission electron microscopy (TEM) characterization was carried out at ICMPE using a FEI Tecnai G2 F20 S-Twin microscope operating at voltage of 200 kV. Chemical composition of the nanostructured InSb anode was determined using a

windowless EDAX Octane Optima 60 mm^2 EDX (Energy Dispersive X-Ray Spectroscopy) analyzer. Surface compositional analysis of the InSb electrodes before and after cycling was conducted by *ex situ* XPS using a Kratos Axis Ultra DLD spectrometer with a monochromatic Al Kα excitation (1486.7 eV) at 150 W and a charge compensation system. The individual core level spectra were collected at an analyzer pass energy of 40 eV. The XPS spectra were calibrated using the standard adventitious C 1s peak at 284.8 eV. XPS spectra were analyzed using a nonlinear Shirley-type background.[51] The core peaks and areas were fitted by a weighted least-squares fitting method using Lorentzian line shapes. To avoid exposure of the sample to air, cycled samples were transferred from the glove box to the XPS chamber of the spectrometer using a sample transfer vessel.

RESULTS AND DISCUSSION

Structure, morphology, and surface composition of pristine nanostructured InSb

The XRD pattern and the profile matching of the InSb compound synthesized via a chemical synthesis route[49] is shown in Figure 1(a) and Figure S2 respectively. The pattern depicts the formation of a cubic phase corresponding to the expected InSb compound with crystallographic parameters matching with reported data ($F\bar{4}3m$, a = 6.476 Å).[52] Reflections corresponding to the precursors are not observed, suggesting the formation of a pure InSb phase. However, two extra reflections with low intensity (at 12.9° and 18.8°) suggest the presence of Sb_2O_3 as a minor impurity, indicating the oxidation of a trace of antimony obtained from the reduction of precursors. The average crystallite size of the as-obtained cubic InSb, estimated by Scherrer method,[53] is 80 nm. However, this value is only an estimation, limited by the hypothesis of spherical symmetry of the crystallites.

The morphological aspects of the as-prepared InSb compound were examined by SEM (Figure 1(b)). As shown in Figure 1(b), the InSb powder is composed of polydispersed primary particles with a size distribution from 1 to 10 µm. Interestingly the micrometric aggregates are however

constituted of nanometric subparticles having a size varying from 20 to 200 nm, as illustrated from the TEM image in Figure 1(c). The as-prepared InSb powder appears as an intrinsic hierarchical assembly of nanostructures into aggregates at the micrometric scale. The high resolution TEM (HRTEM) image in Figure 1(d) shows the high crystalline nature of InSb particles, with various crystalline orientations and crystallites ranging from 20 to 50 nm. This value is close to the mean value of 80 nm estimated from the XRD reflections. In addition, the HRTEM image reveals for example a d-spacing of 3.7 Å, attributed to the (111) crystal plane of the InSb, concordant with the XRD results. The elemental distribution of In, Sb, Zn, and O in the nanostructured InSb powder was determined by EDX, as shown in Figure S3. In and Sb elements are uniformly distributed throughout the particles (Figure S3(b,c)). A large amount of oxygen is detected at the surface of the particles (Figure S3), which suggests an oxidation of the surface. We also note the presence of elemental Zn coming from some metallic Zn or $ZnCl_2$ traces, which likely arised from an uncompleted reaction or incomplete sample filtration during the synthesis.

Surface and morphological characterizations of the as-synthesized InSb powder highlight the peculiar structure of the powder, with a clear aggregation of InSb nanoparticles into larger micrometric structures. This hierarchical assembly should take advantage of the nanometric size of the primary particles to alleviate volume expansion and favor fast reactions, while limiting reactivity with the electrolyte with its micrometric structure.

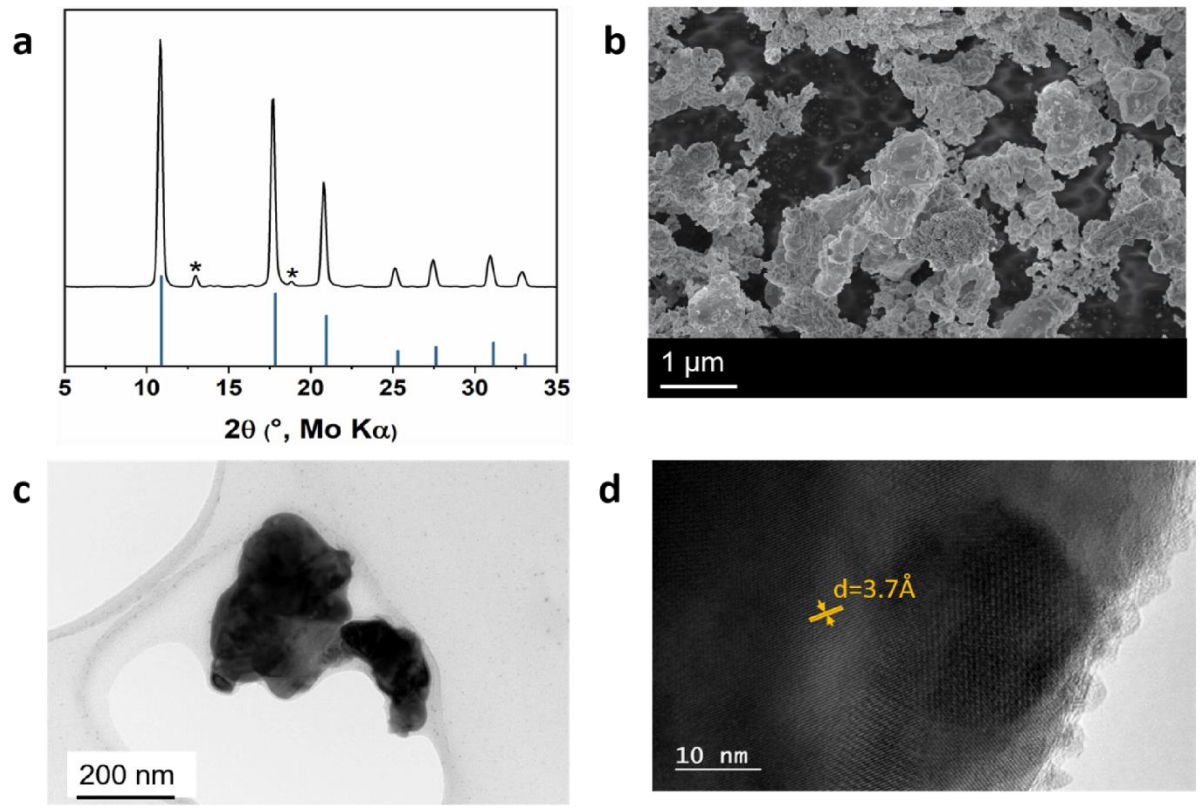

Figure 1. (a) XRD pattern of the as-synthesized nanostructured InSb powder along with its Bragg positions represented by blue vertical bars. Asterisks (*) represent the Sb_2O_3 impurity positions. (b) SEM, (c) TEM, and (d) HRTEM images of the intrinsically nanostructured InSb intermetallic compound.

The surface chemical composition of the as-prepared nanostructured InSb was assessed by means of XPS (Figure 2). Figure 2a depicts a typical XPS survey spectrum of InSb which displays mainly the presence of peaks corresponding to Sb3d, In3d and C1s. The high resolution C1s core spectrum (Figure 2b) shows three peaks at 284.8, 286.0, and 289.0 eV, which are attributed to C-C/C-H, CO, and CO_2 environment, respectively. These carbon compounds arise from hydrocarbon contamination, always present at the extreme surface. As seen from the O1s/Sb3d core spectrum (Fig. 2c), a set of doublet with low intensity located at 527.8 ($Sb3d_{5/2}$) and 537.0 eV ($Sb3d_{3/2}$) is detected and ascribed to the expected InSb compound.[54] A second doublet is detected at a slightly higher binding energy (530.3 and 539.7 eV), representing a higher oxidation state of Sb (+5). It is assigned to Sb_2O_3, resulting from the oxidation of the

InSb surface.[55] In the In3d spectrum of the as-prepared InSb (Figure 2d), two main components are clearly observed: InSb and In_2O_3, located at 444.1 ($3d_{5/2}$) and 444.7 eV ($3d_{5/2}$) respectively. Consistent with Sb_2O_3, the higher binding energy peak at 444.7 eV corresponds to In_2O_3 from the oxidation of the InSb surface. Note that the broad O1s peak at 531.5 eV is attributed to the combined contributions of Sb_2O_3, In_2O_3, and CO/CO_2 components.

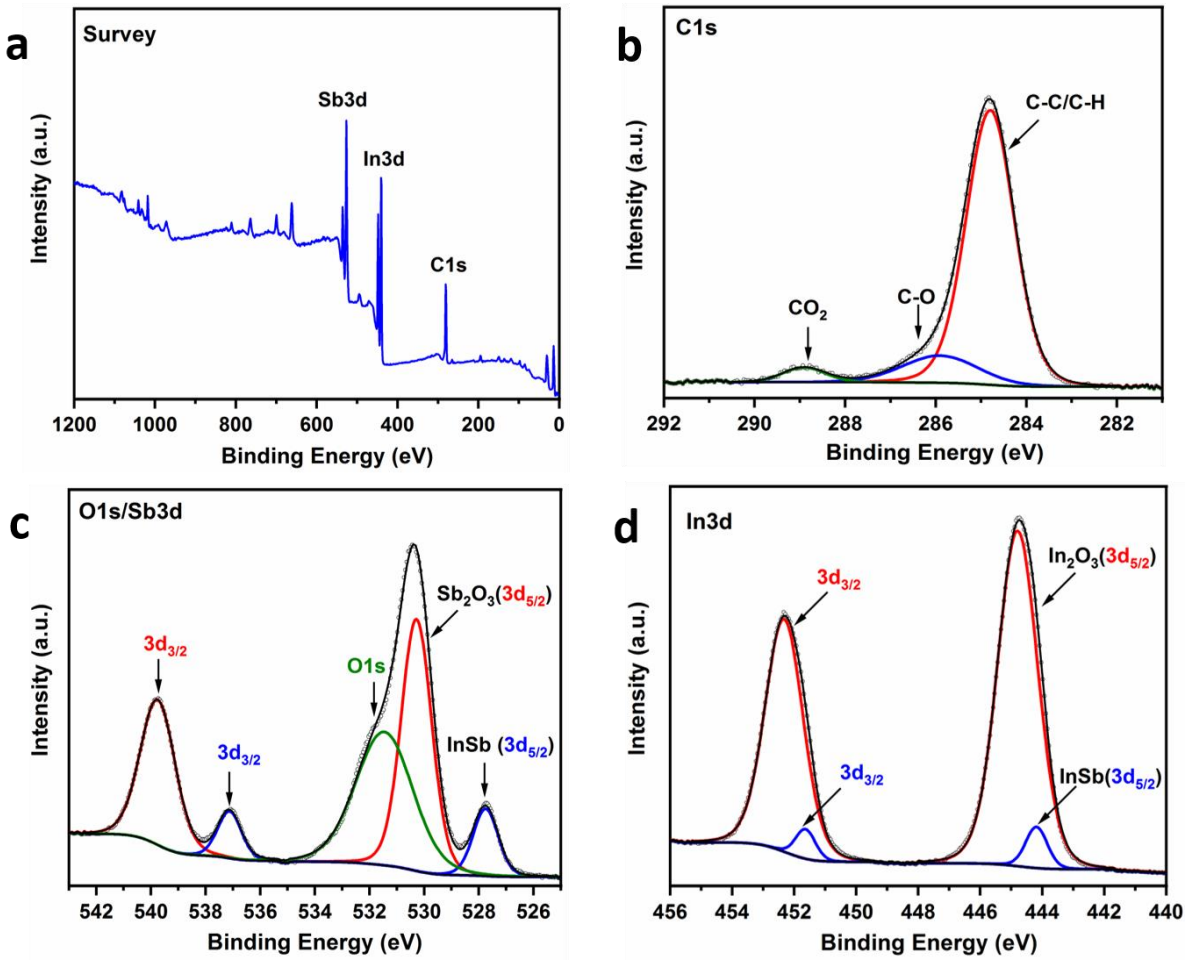

Figure 2. Detailed XPS chemical compositional characterization of the as-prepared InSb powder. (a) Survey, (b) C1s, (c) O1s/Sb3d, and (d) In3d XPS spectra. All the spectra were calibrated by adjusting the C1s (C-C/C-H) peak at 284.8 eV.

Electrochemical performance of the nanostructured InSb electrode

The electrochemical properties of the nanostructured InSb alloy were investigated by performing CVs and galvanostatic discharge-charge measurements. FEC was used as an additive in the conventional EC:DMC electrolyte to stabilize the solid electrode interphase (SEI). The first five CV curves at a sweep rate of 0.1 mV s^{-1} are presented in Figure 3a. During the first cathodic scan, a broad peak at 0.75 V_{Na} (V_{Na} as V vs Na^+/Na) appears, which can be ascribed to the formation of a SEI film, followed by a second strong peak at 0.15 V_{Na}, attributed to the sodiation process of InSb with Na ($InSb + (x+y)Na^+ + (x+y)e^- \rightarrow Na_xSb + Na_yIn$, $x \leq 3$ and $y \geq 1$).[56] In the anodic scan, two broad peaks centered at 0.45 and 0.80 V_{Na} are identified, corresponding to the reversible desodiation processes. In the second cathodic scan, two peaks at 0.51 and 0.30 V are related to the expected sodium alloying with InSb to form Na_xSb ($x \leq 3$) and Na_3Sb, respectively,[57] and a third peak at 0.11 V is ascribed to the formation of Na_yIn ($y \geq 1$) during the sodiation process. In the second anodic scan, two peaks at 0.80 and 0.47 V refer to the desodiation reaction of Na_xSb/Na_3Sb and Na_yIn, respectively. From the subsequent scan onwards, the CVs profiles are significantly overlapping regardless of slight change in potential, indicating the good stability of the electrodes. In addition, CV measurements were performed at different scan rates (Figure S4) to get insights on kinetics for InSb and on a possible pseudocapacitive behavior. The capacitance analysis show that the electrochemical reactions are diffusion-limited (b ~0.64), which implies a battery-like process and not a capacitance-controlled process.

Figure 3(b,c) exhibits the galvanostatic discharge−charge profiles of the InSb electrode obtained at current rate of C/5 and 1C. Both discharge-charge profiles present a similar shape. In the first discharge, only one voltage plateau is observed, while the subsequent discharge profiles consist in three voltage plateaus. The first discharge plateau is occurring at a lower voltage compared to the following cycles, which is often characteristic of the behavior of alloys.

The presence of the three plateaus corroborates the CV results and implies some biphasic processes, suggesting again formation of Na_xSb and Na_yIn, most probably the NaIn phase based on the sodiation of pure In.[58] Similar to the CVs results, the discharge−charge profiles of the 2nd and 50th cycles are substantially coinciding, highlighting the excellent stability of the InSb material over long cycling. As expected from the lithiation and magnesiation of InSb, the sodiation of nanostructured InSb proceeds first at higher voltage through the alloying with Sb and is followed at a lower voltage to the reactivity with In.

The InSb electrode delivers a first discharge capacity of 545 mAh g^{-1} at C/5 (~110 mA g^{-1}) (Figure3b), which is higher than the theoretical specific capacity of InSb (453 mAh g^{-1}, assuming a 4-electron transfer per InSb unit). Concerning the first charge, a capacity of 440 mAh g^{-1} is reached, which corresponds to an initial coulombic efficiency of 80 %. We consider that this irreversible capacity is related to the irreversible formation of the SEI from electrolyte decomposition (Figure 3b). In the second cycle, the discharge capacity amounts to 453 mAh g^{-1}, similarly to the theoretical value. The capacity is noticeably stable around 450 mAh g^{-1} for 50 cycles at C/5 (~ 110 mA g^{-1}), while a capacity of 430 mAh g^{-1} was achieved for the previously reported ball-milled InSb, yet at a more than two times slower rate (50 mA g^{-1}) at 30°C in a ionic liquid electrolyte.[48] It is noteworthy that after the first cycle, the coulombic efficiency increases to 96 % and accelerates to >99 % in the second and following cycles, respectively. The rapid stabilization of the coulombic efficiency denotes a quick and efficient stabilization of the SEI on the InSb surface. At high current like 1C (~570 mA g^{-1}), the InSb electrode delivers a first high discharge capacity of 426 mAh g^{-1}. This value represents 90 % of the theoretical specific capacity of InSb. In this case, the initial coulombic efficiency amounts to 85 % at 1C (slightly higher than the C/5 case). The InSb electrode exhibits a discharge capacity of 362 mAh g^{-1} after 100 cycles at 1C, which represents a remarkable capacity retention of 96 %. The above electrochemical performances of the InSb electrodes suggest that

the nanostructured InSb is definitely a promising host for reversible sodium storage and compete with ball-milled InSb and other alloy-based materials in literature (Table S1). The excellent sodium storage performances can be ascribed to the efficient synergetic coupling of In and Sb and to the hierarchical nano/micro structure of the InSb material.

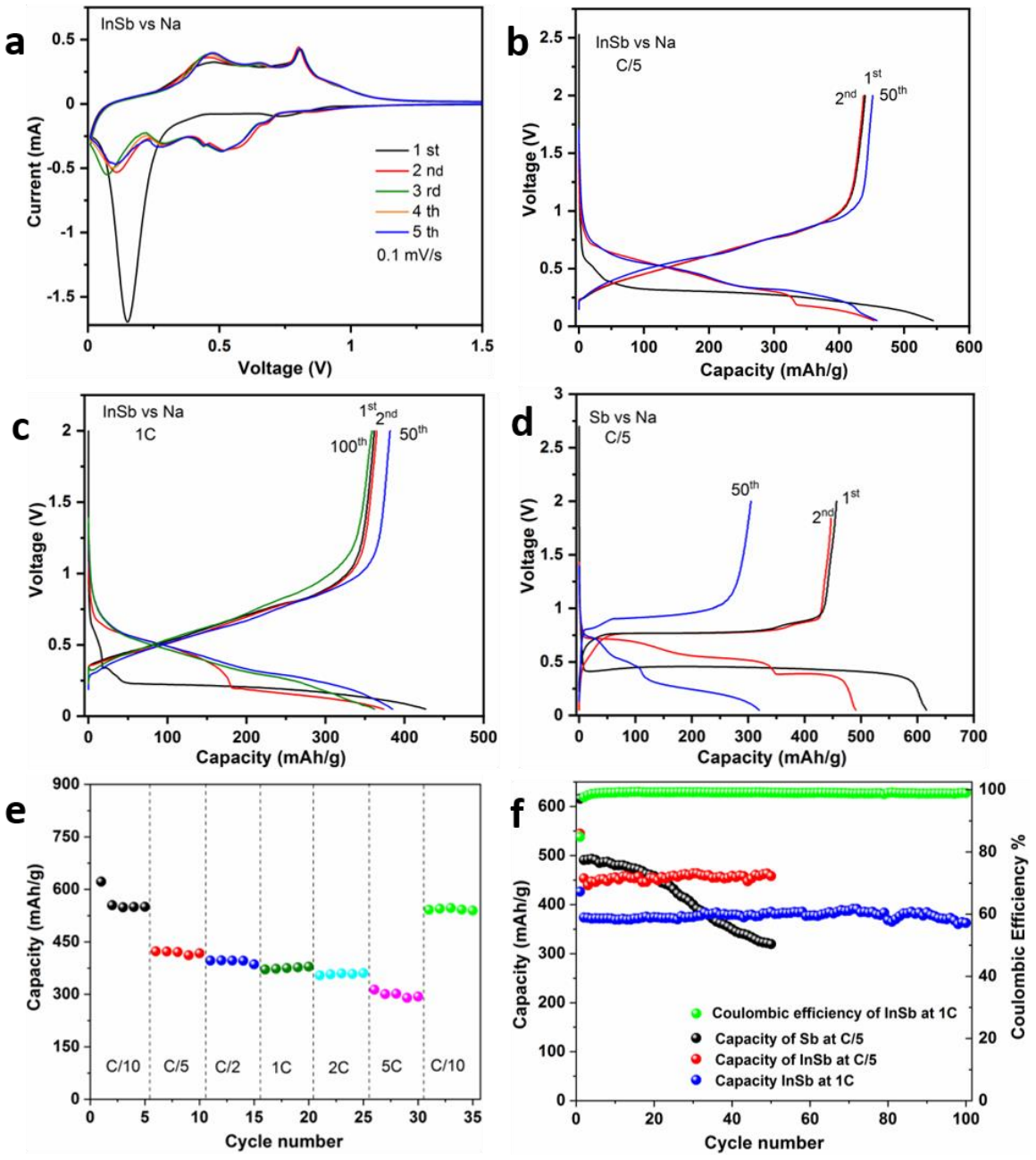

Figure 3. (a) CVs of a InSb electrode for the first five cycles at a scan rate 0.1 mV s^{-1} over a potential window of 1.5 V-0.01 V. (b-c) Discharge/charge voltage profiles of nanostructured InSb electrodes at different cycle number at a current rate of (b) C/5 and (c) 1C. (d)

Discharge/charge voltage profiles of a nanostructured Sb electrode at a current rate of C/5. (e) Rate capability of the InSb electrode at various current rates ranging from C/10 to 1C. (f) Cycling performance of nanostructured InSb (C/5 and 1C) and nanostructured Sb (C/5) and corresponding coulombic efficiency of nanostructured InSb at 1C. The electrolyte was cycled in 1 M $NaClO_4$ in EC:DMC electrolyte with 5% FEC additive.

To unveil the benefit of In and Sb coupling, we compared the electrochemical performance of nanostructured InSb with a nanostructured Sb produced with the same synthesis protocol. Figure 3(d) depicts discharge/charge profiles of nanostructured Sb electrode for the 1st, 2nd and 50th cycles between 0.05–2.0 V at C/5 rate. The Sb electrode provides a discharge capacity of 616 mAh g^{-1} in the first cycle, close to the theoretical value of 660 mAh g^{-1}. In contrast to the InSb electrode, a capacity decay with cycling is observed for the Sb electrode, most probably due to the pulverization of Sb by large volume change. In comparison to Sb electrode, it is worth noting that the cycle stability is significantly improved when In and Sb are combined in a homogeneous alloy, which evidently reveals a strong synergy between the two metals. We suggest that the intermetallic matrix can alleviate more easily the mechanical stress developed during sodiation/desodiation processes.

Figure 3e shows the high rate performance of the as-prepared nanostructured InSb electrode at various current rates varying from C/10 to 5C. The InSb electrode displays a discharge capacity of 554 (2nd cycle), 397, and 313 mAh g^{-1} at C/10, C/2, and 5C, respectively. Even at a higher current density of 2C and 5C, high capacities are maintained, demonstrating that InSb can sustain high C-rates. Interestingly, a high capacity of 541 mAh g^{-1} is recovered when the current rate is shifted back from 5C to C/10, indicating strong electrochemical stability. Figure 3(f) demonstrates the cycling performance of the InSb electrode at 1C (~570 mA g^{-1}), while the cycling performance of the Sb electrode is also given for comparison. The InSb electrode

exhibits an impressive stability for a hundred cycles at this high rate with a capacity around 370 mAh g^{-1}. The capacity is very stable for the InSb electrode at both current rates (C/5 and 1C), while the profiles for Sb electrode starts falling after few cycles. Despite the lower capacity of InSb compared to Sb in the initial cycles, the capacity becomes higher than the Sb after 33 cycles at C/5 (10 cycles at 1C). After 50 cycles, the Sb electrode shows a discharge capacity of 319 mAh g^{-1}, suggesting a capacity retention of only 64 %, while the capacity retention is close to 100 % at both current rates for InSb (C/5 and 1C). Thus, nanostructured InSb as a negative electrode provides superior performance in terms of performance stability and rate capacity. The presence of the FEC additive in the electrolyte plays without doubt a role in the cycling stability of the InSb electrode,[59] but its presence is not sufficient to stabilize the capacity in the case of nanostructured Sb.

The outstanding electrochemical performance of the InSb electrode can be attributed to two main features: 1) the synergetic effect in the InSb intermetallic compound and 2) the singular hierarchical assembly of nanostructured InSb into micrometric aggregates. The latter offers limited reactivity with the electrolyte compared to well-defined nanoparticles and a unique structure that not only buffers the volume expansion but also facilitates ions and electrons transport, leading to high rate capability.

Secondly, the quick capacity fading for Sb electrode case can be due to the pulverization of Sb during sodiation/desodiation processes,[60] while the synergistic effect between In and Sb in the alloy matrix could release the mechanical strain induced during the sodiation/desodiation process. We calculated that the theoretical volume expansion of In to form NaIn is around 115%, while the theoretical volume expansion of Sb to form Na_3Sb is ~300% (see Table S2). InSb will thus take benefit of the relatively low volumetric expansion of In as compared to other alloys. Moreover, we can infer that the sodiated phases created at different voltages and the phase boundaries between the Na_3Sb and Na_yIn phases can improve the volume

accommodation, resulting in excellent cycling stability. Further post-mortem investigations, such as SEM, are needed to confirm the better volume alleviation of nanostructured InSb in comparison with nanostructured Sb, and will be reported later.

Interfacial and resistance behavior of InSb electrode during cycling

The evolution of the electrode surface composition of the nanostructured InSb after cycling in a carbonated electrolyte with FEC as additive was evaluated for the first time by *ex situ* XPS. Figure 4(a-f) depicts the XPS spectra (C1s, O1s/Sb3d, In3d, F1s, Na1s, and Cl2p) of InSb electrodes after the initial discharge and charge in the FEC-based electrolyte. In the C1s spectra, four major peaks are observed for the pristine InSb composite electrode (InSb/C/CMC) (Figure 4a), in which two peaks at 287.0 and 288.5 eV are related to the CMC binder.[61] The other two peaks centered at 284.8 and 285.0 eV are characteristic of C-C/C-H and C=C environments, which are attributed to aliphatic chains and carbon additives, respectively. Two minor peaks situated at 286.0 and 289.0 eV are indexed to C-O and CO_3, respectively. After a complete discharge, the peaks related to active material, CMC binder and carbon additives are no longer detected, suggesting the formation of a SEI layer (> 5 nm in thickness, depth limit of XPS measurement) on the electrode surface. In the C1s spectrum of the discharged sample, an increase in relative intensities of the peaks corresponding to C-C/C-H, C-O, CO_2, and CO_3 environments is observed.[62] These carbon containing components can be attributed to the species usually present in the SEI derived from a EC/DMC based electrolyte.[63] After the first charge, the intensity of the CO_3/CO_2, C-O, and C-C/C-H peaks decreases significantly, and the peak related to the carbon additives reappears, suggesting a possible partial dissolution of the SEI. In the XPS Sb3d/O1s core spectrum (Figure 4b), three components are clearly observed for the pristine electrode: InSb (527.0, 536.0 eV), Sb_2O_3 (530.3, 539.7 eV), and CMC (533.4 eV). After the first discharge, these components are not observed, indicating again the formation of a thick SEI layer. Two new features related to Na-Auger and $NaClO_4$ salt are observed at

533.0 and 526.0 eV, respectively. The active material InSb is recovered in the Sb3d spectrum after the charge, suggesting that InSb is formed again after full desodiation, in contrast to the phase segregation of In and Sb observed for ball-milled InSb.[48] Moreover this corroborates also the dissolution of the SEI layer. The phenomenon of SEI dissolution for the InSb electrode in Na-ion cell is consistent with reported literature for Sb based electrodes.[55,64]

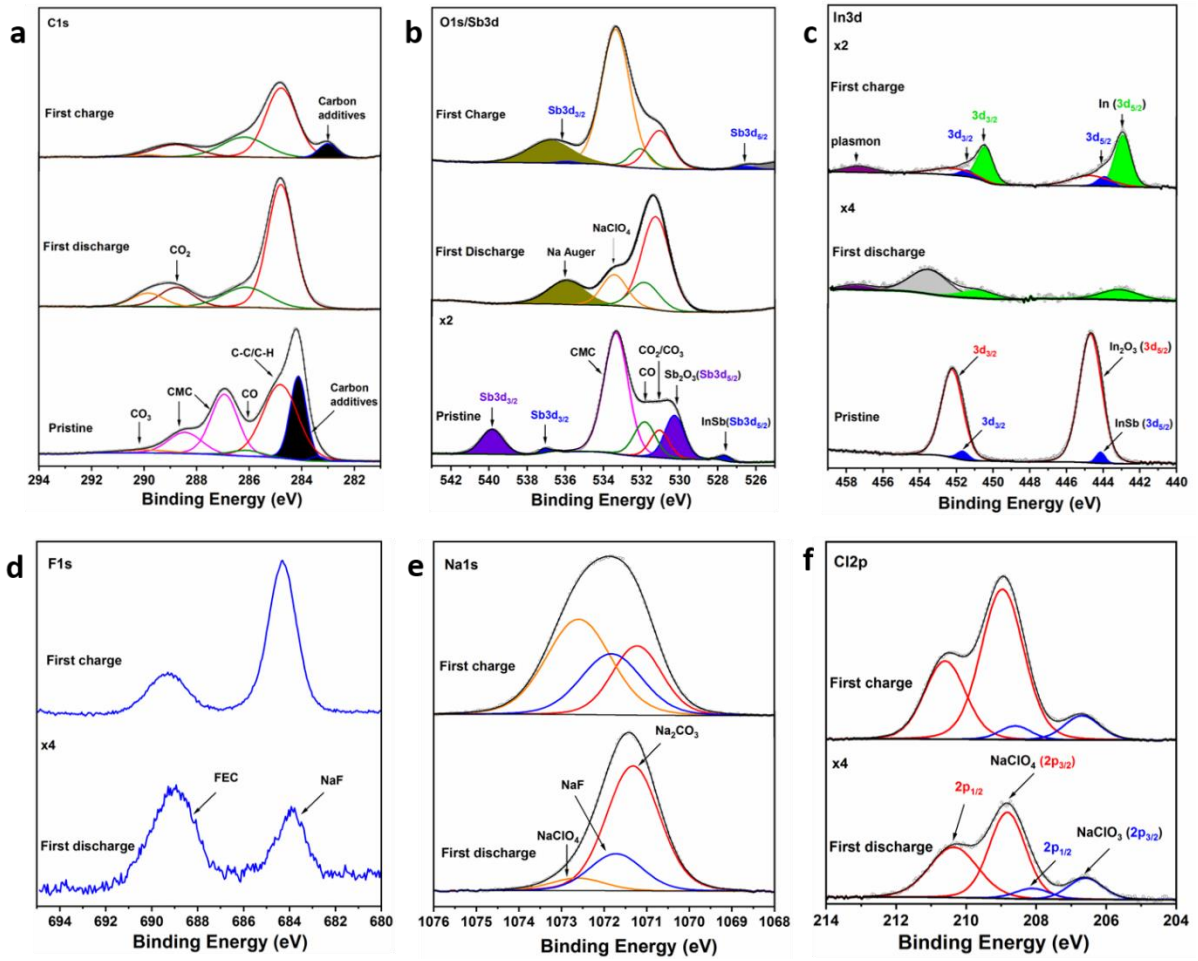

Figure 4. (a) C1s, (b) O1s/Sb3d, (c) In3d, (d) F1s, (e) Na1s, and (f) Cl2p XPS spectra of InSb electrodes cycled in 1 M $NaClO_4$ in EC:DMC electrolyte with 5% FEC additive. All the spectra were calibrated by adjusting C1s (C-C/C-H) peak at 284.8 eV.

In the In 3d core spectrum, only very weak signals are observed for the discharged sample (Figure 4c), suggesting formation of metallic In. The very low intensity of peaks indicates a nearly total covering of active material by the SEI layer. Some peaks with low intensity are

detected in the charged sample spectrum due to the partial dissolution of the protective layer. A set of doublet peaks corresponding to In metal is observed in the lower binding energy region (443.1, 450.8 eV). The appearance of In component is intuitively puzzling as the formation of metallic In was not anticipated in the charged electrode, but this time in agreement with the reactivity of ball-milled InSb.[48] Few traces of In might have resulted from a side reaction during the desodiation process or from the extrusion of In from InSb upon sodiation of Sb, as already observed in the magnesiation and lithiation of InSb.[46,47] XPS analyses using depth profiling to specifically etch the SEI layer would be further implemented to probe the phases formed upon magnesiation of InSb. The XPS F1s core spectrum (Figure 4d) is characterized by two main components at 689.0 eV and 684.0 eV, attributed to FEC and NaF, respectively. The deposition of NaF on the electrode surface in the presence of FEC is consistent with previous observation for Sb based electrodes.[64,65] Both species are formed after discharge and increased significantly after charge, revealing the continuous decomposition of FEC during cycling. The presence of NaF in the SEI layer seems to play a role in the capacity stability, as generally observed for Sb-based electrodes. Concerning the Na1s core spectrum (Figure 4e), three Na signals from the Na_2CO_3 (1071.3 eV), NaF (1071.7 eV), and $NaClO_4$ (1072.8 eV) components are observed. Finally, the Cl2p spectra suggest a slight decomposition of $NaClO_4$ salt into $NaClO_3$ at the surface of the electrode (Figure 4f).[64] Unlike other SEI species, $NaClO_3$ does not seem to re-dissolve after the first charge. Note that the peaks corresponding to NaCl salt are not detected here, in contrast to Sb electrodes.[55]

To sum up, a typical composition of the SEI layer is formed at the InSb surface. A thick SEI layer consisting of hydrocarbon species, carbonates, and degradation products of solvents and electrolyte are observed. Some organic species containing C-C/C-H, C-O, CO_2, and CO_3

environments have been partially removed after the charge process. In contrast, components like NaF and $NaClO_3$ do not dissolved after the charge.

To further understand the superior stability of InSb electrode, EIS measurements were performed on a InSb electrode before and after cycling, as shown in Figure 5a. An equivalent circuit was used for fitting the impedance spectrum (Figure 5b). R_1 is the bulk resistance of the cell, which represents the combined resistances of the electrolyte, separator and electrodes. R_2 and Q_2 are charge-transfer resistance and related double-layer capacitance, respectively,[66] while W_2 is the Warburg impedance related to diffusion of ions in the host materials. Usually, an impedance spectrum for a half-cell consists of two semicircles at high frequency, attributed to interfacial and charge transfer resistance, and one tilted straight line at low frequency corresponding to ionic diffusion within active material. In contrast, the impedance spectra for InSb electrode shows only one semicircle corresponding to the charge transfer resistance and a tilted straight line related to sodium diffusion process. The absence of second semicircle suggests that the conductivity mechanism is dominated by the charge transfer resistance. A charge transfer resistance (R_2) of 907 Ω is obtained for the electrode at OCV, which is related to a native passivation of the electrode. After 10 and 20 cycles, the charge transfer resistance value decreases to 25 and 35 Ω, respectively. The significant decrease of the resistance upon cycling reveals the increase of the electrochemical activity for the InSb electrode. The resistance value retains to be in the same order even after 50 cycles, i.e. 36 Ω, indicating strong structural stability of the electrode. This above results further demonstrate that the synergy created inside the InSb compound leads to rapid electron transfer, fast reaction kinetics, and structural integrity, attesting excellent electrochemical performance.

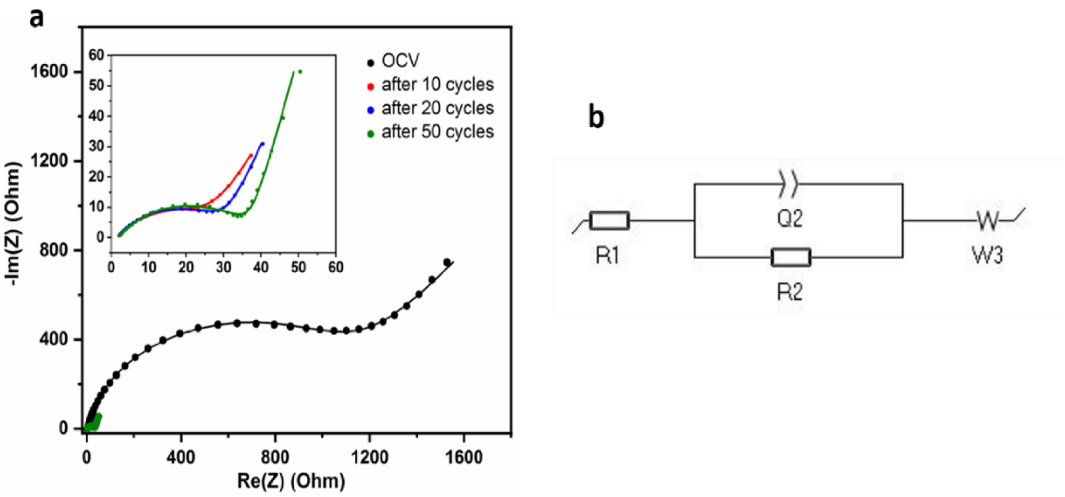

Figure 5. (a) Nyquist plots of a InSb electrode in Na–ion half-cell before and after 10, 20 and 50 cycles. The inset shows the semicircles in high frequency region. Dots represent the measured data and the solid line the fitted data. (b) Equivalent circuit model used for fitting the impedance diagram.

Electrochemical sodiation mechanism in the InSb intermetallic compound

To get insight into the sodiation mechanism and the phases evolution of the InSb electrode, operando XRD analysis was carried out in voltage range of 2.3−0.05 V_{Na} during the first discharge process at C/40, as shown in Figure 6a,b. At the beginning of the discharge, the main reflection peaks located at 10.9°, 17.7° and 20.8°, are attributed to the InSb phase. The Bragg positions at 22.8°, 23.5° and 30.8° are assigned to the beryllium window (Figure 6a). With continuous discharging in the voltage range of 2.3−0.4 V_{Na}, the intensity of peaks corresponding to InSb remain unchanged, but their Bragg position are shifted to higher 2θ values, implying a possible intercalation of Na into the InSb lattice, i.e. Na_xInSb. In this next stage, despite a significant advance in the sodiation reaction, no new peak appears, implying that intermediate Na_xSb could be formed in an amorphous state at this stage of discharge, which is in good agreement with previous studies.[57,67] Upon further discharging (0.3−0.05 V_{Na}), the peaks corresponding to the InSb phase begin to weaken. At the same time, there is a gradual increase

of broad peaks located at around 10°, 16°, and 19°, which are assigned to Na_3Sb and NaIn phases.[48,57,68] These phases seem to form in a poorly crystalline state, as already observed for ball-milled InSb upon sodiation.[48] After the end of discharge (figure 6a,b), when most of the electrode material is sodiated, the InSb characteristic peaks significantly vanished and the broad features corresponding to Na_3Sb and NaIn are intensified.

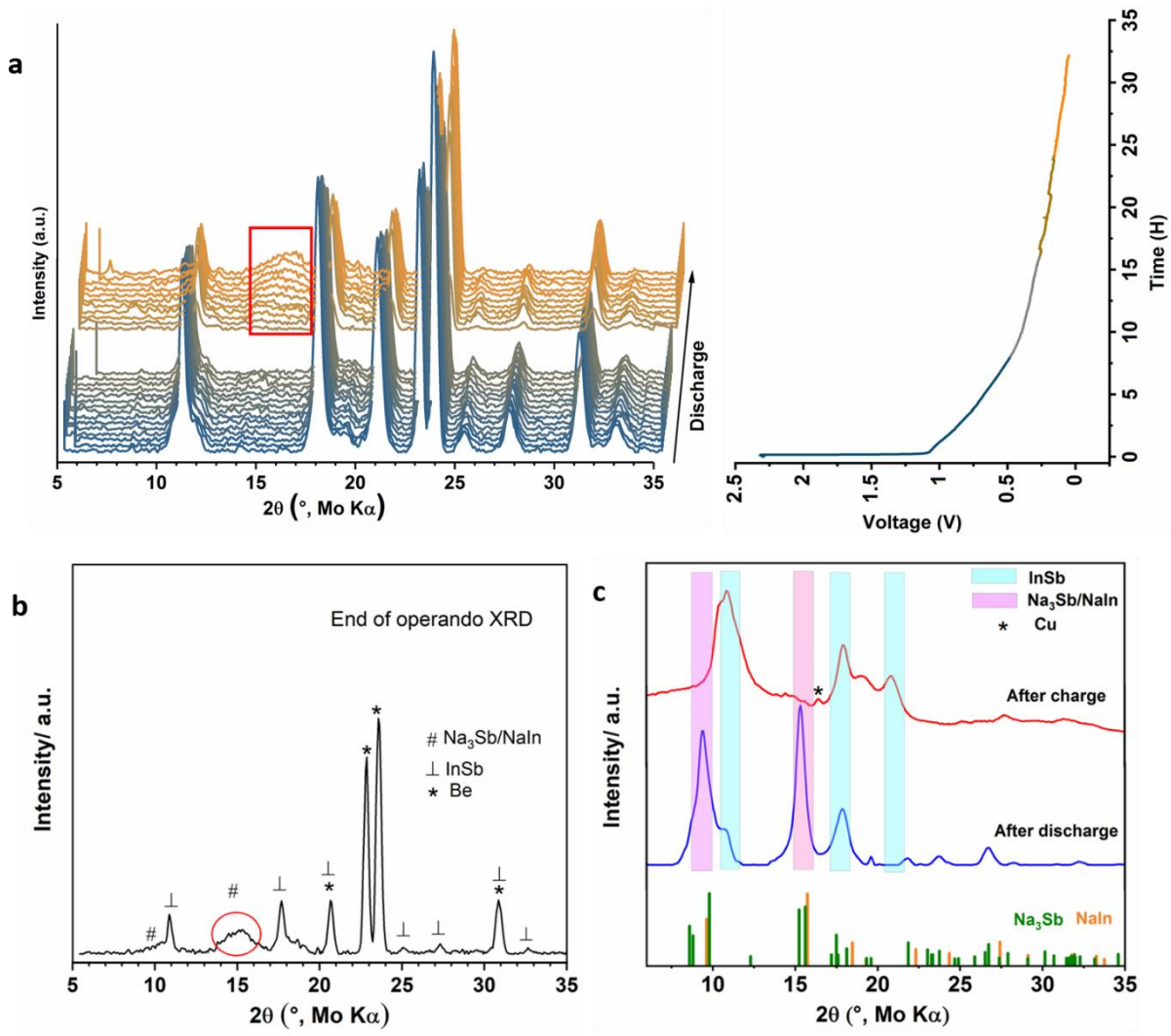

Figure 6. (a) Line plot of the *operando* XRD results of a nanostructured InSb auto-supported electrode during the discharge process at a current rate of C/40 (note that no acquisition was acquired during the middle of discharge due to a technical beam shutdown) and corresponding discharge profile of the InSb electrode are also shown for reference (Right part). (b) XRD pattern extracted from figure (a) for the end of operando measurement (end of discharge). (c)

Ex situ XRD pattern of the InSb electrode after a complete discharge and charge at a current of C/10.

To further investigate the mechanism of the proposed sodiation reaction of the InSb electrode, ex situ XRD was performed on nanostructured InSb electrodes after discharge and charge, as shown in Figure 6c. In contrast to the *operando* measurement, after a complete discharge, two intense peaks located at 9.4° and 15.3° are observed, which attests the presence of Na_3Sb in a crystalline state on the *ex situ* sample.[18,57] Two more peaks (10° and 15.6°) barely separated from the Na_3Sb peaks can be assigned to the NaIn phase.[68] In contrast to the *operando* measurement where poorly crystalline phases are observed, the peaks of the newly formed phases are well-defined, suggesting crystalline phases. This also contrasts strongly with the results obtained on ball-milled InSb, where poor crystalline phases were observed, and the presence of Na_3Sb and NaIn only implicitly suggested from the electrochemical measurements.[48] After a full charge, the typical peaks associated to Na_3Sb/NaIn phases disappeared, while characteristic peaks of InSb reappeared, evidencing here clearly that the InSb compound is regenerated after a full sodiation/desodiation cycle. This electrochemical behavior differs substantially from the study from Usui et al.,[48] where a phase segregation generating In and Sb is observed for ball-milled InSb.

Operando and *ex situ* XRD measurements, combined with the electrochemical measurements described above, hint at the following two-step processes for the sodiation of nanostructured InSb, i.e. formation of Na_3Sb and NaIn during the sodiation process of InSb via the intermediate Na_xInSb and that In and Sb reunite to form InSb upon full desodiation:

$$InSb + xNa^+ + xe^- \leftrightarrow Na_xInSb$$

$$Na_xInSb + (4-x)Na^+ + (4-x)e^- \leftrightarrow Na_3Sb + NaIn$$

Yet, the discrepancies between the *operando* and *ex situ* measurements underline the possible complex sodiation and desodiation mechanism of the InSb phase that may involve non-trivial successive phase amorphization and crystallization processes. Further studies will focus on the in-depth investigation of the reactivity of InSb upon sodiation and desodiation.

CONCLUSIONS

Herein, we have demonstrated the promising performance of nanostructured InSb as a negative electrode for sodium-ion batteries. The InSb compound was successfully synthetized in the form of micrometric aggregates intrinsically nanostructured. The synergy created between In and Sb and the benefit of nanostructuring for the InSb intermetallic compound is clearly evidenced. Remarkably, coupling In and Sb in nanostructured InSb improves greatly the stability of the capacity along cycling in comparison to nanostructured Sb alone. The InSb electrode delivers a promising stable capacity of 450 mAh g^{-1} for 50 cycles at C/5 and 365 mAh g^{-1} for 100 cycles at 1C, outperforming the performance of ball-milled InSb very recently reported. Based on volume expansion values of In and Sb, we propose that the combination of In and Sb in InSb helps alleviating the strong mechanical stress and volume change upon sodiation, leading to more efficient sodiation/desodiation processes and a stable SEI.

XPS revealed that the SEI on the InSb is based on FEC and salt degradation products such as NaF and $NaClO_3$. Some organic species from carbonates degradation are also evidenced, yet they partially dissolve on charge. While we identified the SEI composition on the InSb electrode, our XRD analyses give a glimpse of the complex alloying mechanisms of InSb upon sodiation and desodiation, by evidencing formation of Na_3Sb and NaIn and formation of InSb after full desodiation. Yet, discrepancies between *operando* and *ex situ* measurements hint at some more complex mechanisms involving amorphization. A detailed investigation, notably through *operando* and/or *ex situ* XRD and/or X-Ray absorption spectroscopy, is needed to assess if the reactivity of InSb follows only the mechanisms of pure In and Sb metals, or if more

peculiar phase transformations occur. A better understanding of the mechanisms will without doubt unveil the critical characteristics of nanostructured InSb behind its promising performance. Overall, this study demonstrates how important the exploration of alloys and nanostructuration still is to improve further their reactivity and move towards viable high-capacity negative electrodes for Na-ion batteries.

ACKNOWLEDGMENTS

This work was supported by the program of ANR-16-CE05-0004 from Agence Nationale de la Recherche (ANR), France. Jim Hoarau is acknowledged for the design and machining of the XRD *operando* cell.

ASSOCIATED CONTENT

Supporting information. Schematic diagram of the synthesis process, refined XRD pattern of the InSb compound, EDX-SEM images of InSb powder, Table comparing performance of Sb-based alloys, Table for theoretical volume expansion of Na-M compounds.

CONFLICTS OF INTEREST

There are no conflicts to declare.

AUTHOR INFORMATION

Corresponding Author

* irshad.mohammad@cea.fr; magali.gauthier@cea.fr

REFERENCES

1 J. W. Choi and D. Aurbach, *Nature Reviews Materials*, 2016, **1**, 1–16.
2 F. Risacher and B. Fritz, *Aquatic Geochemistry*, 2009, **15**, 123–157.
3 A. Yaksic and J. E. Tilton, *Resources Policy*, 2009, **34**, 185–194.
4 M. D. Slater, D. Kim, E. Lee and C. S. Johnson, *Advanced Functional Materials*, 2013, **23**, 947–958.
5 I. Hasa, S. Mariyappan, D. Saurel, P. Adelhelm, A. Y. Koposov, C. Masquelier, L. Croguennec and M. Casas-Cabanas, *Journal of Power Sources*, 2021, **482**, 228872.

6 V. L. Chevrier and G. Ceder, *J. Electrochem. Soc.*, 2011, **158**, A1011.
7 D. Aurbach, Z. Lu, A. Schechter, Y. Gofer, H. Gizbar, R. Turgeman, Y. Cohen, M. Moshkovich and E. Levi, *Nature*, 2000, **407**, 724–727.
8 R. Dominko, J. Bitenc, R. Berthelot, M. Gauthier, G. Pagot and V. Di Noto, *Journal of Power Sources*, 2020, **478**, 229027.
9 M.-C. Lin, M. Gong, B. Lu, Y. Wu, D.-Y. Wang, M. Guan, M. Angell, C. Chen, J. Yang, B.-J. Hwang and H. Dai, *Nature*, 2015, **520**, 324–328.
10 R. J. Gummow, G. Vamvounis, M. B. Kannan and Y. He, *Advanced Materials*, 2018, **30**, 1801702.
11 A. Eftekhari, *Journal of Power Sources*, 2004, **126**, 221–228.
12 M. A. Reddy and M. Fichtner, *J. Mater. Chem.*, 2011, **21**, 17059–17062.
13 I. Mohammad, R. Witter, M. Fichtner and M. Anji Reddy, *ACS Appl. Energy Mater.*, 2018, **1**, 4766–4775.
14 M. A. Nowroozi, I. Mohammad, P. Molaiyan, K. Wissel, A. R. Munnangi and O. Clemens, *J. Mater. Chem. A*, , DOI:10.1039/D0TA11656D.
15 X. Zhao, S. Ren, M. Bruns and M. Fichtner, *Journal of Power Sources*, 2014, **245**, 706–711.
16 B. L. Ellis and L. F. Nazar, *Current Opinion in Solid State and Materials Science*, 2012, **16**, 168–177.
17 V. Palomares, P. Serras, I. Villaluenga, K. B. Hueso, J. Carretero-González and T. Rojo, *Energy Environ. Sci.*, 2012, **5**, 5884–5901.
18 M. He, K. Kravchyk, M. Walter and M. V. Kovalenko, *Nano Lett.*, 2014, **14**, 1255–1262.
19 N. Yabuuchi, K. Kubota, M. Dahbi and S. Komaba, *Chem. Rev.*, 2014, **114**, 11636–11682.
20 X. Xiang, K. Zhang and J. Chen, *Advanced Materials*, 2015, **27**, 5343–5364.
21 C. Fang, Y. Huang, W. Zhang, J. Han, Z. Deng, Y. Cao and H. Yang, *Advanced Energy Materials*, 2016, **6**, 1501727.
22 Y.-U. Park, D.-H. Seo, H.-S. Kwon, B. Kim, J. Kim, H. Kim, I. Kim, H.-I. Yoo and K. Kang, *J. Am. Chem. Soc.*, 2013, **135**, 13870–13878.
23 D. A. Stevens and J. R. Dahn, *J. Electrochem. Soc.*, 2001, **148**, A803.
24 Y. Wen, K. He, Y. Zhu, F. Han, Y. Xu, I. Matsuda, Y. Ishii, J. Cumings and C. Wang, *Nature Communications*, 2014, **5**, 4033.
25 B. Jache and P. Adelhelm, *Angewandte Chemie International Edition*, 2014, **53**, 10169–10173.
26 A. Rudola, K. Saravanan, C. W. Mason and P. Balaya, *J. Mater. Chem. A*, 2013, **1**, 2653–2662.
27 Y. Zhao, T. Sun, Q. Yin, J. Zhang, S. Zhang, J. Luo, H. Yan, L. Zheng, J. Han and M. Wei, *J. Mater. Chem. A*, 2019, **7**, 15371–15377.
28 C. C. Yang, D. M. Zhang, L. Du and Q. Jiang, *J. Mater. Chem. A*, 2018, **6**, 12663–12671.
29 S. Wang and X.-B. Zhang, *Advanced Materials*, 2019, **31**, 1805432.
30 C. Bommier, W. Luo, W.-Y. Gao, A. Greaney, S. Ma and X. Ji, *Carbon*, 2014, **76**, 165–174.
31 D. Li, L. Zhang, H. Chen, L. Ding, S. Wang and H. Wang, *Chem. Commun.*, 2015, **51**, 16045–16048.
32 W. T. Jing, C. C. Yang and Q. Jiang, *J. Mater. Chem. A*, 2020, **8**, 2913–2933.
33 L. Baggetto, P. Ganesh, R. P. Meisner, R. R. Unocic, J.-C. Jumas, C. A. Bridges and G. M. Veith, *Journal of Power Sources*, 2013, **234**, 48–59.

34 W. Tian, S. Zhang, C. Huo, D. Zhu, Q. Li, L. Wang, X. Ren, L. Xie, S. Guo, P. K. Chu, H. Zeng and K. Huo, *ACS Nano*, 2018, **12**, 1887–1893.
35 S. Liu, J. Feng, X. Bian, J. Liu and H. Xu, *Energy Environ. Sci.*, 2016, **9**, 1229–1236.
36 I. Hasa, S. Passerini and J. Hassoun, *RSC Adv.*, 2015, **5**, 48928–48934.
37 C. Wu, L. Shen, S. Chen, Y. Jiang, P. Kopold, P. A. van Aken, J. Maier and Y. Yu, *Energy Storage Materials*, 2018, **10**, 122–129.
38 R. Ramarajan, M. Kovendhan, K. Thangaraju, D. P. Joseph and R. R. Babu, *Applied Surface Science*, 2019, **487**, 1385–1393.
39 J. Song, P. Yan, L. Luo, X. Qi, X. Rong, J. Zheng, B. Xiao, S. Feng, C. Wang, Y.-S. Hu, Y. Lin, V. L. Sprenkle and X. Li, *Nano Energy*, 2017, **40**, 504–511.
40 W. Ma, J. Wang, H. Gao, J. Niu, F. Luo, Z. Peng and Z. Zhang, *Energy Storage Materials*, 2018, **13**, 247–256.
41 X. Li, M. Sun, J. Ni and L. Li, *Advanced Energy Materials*, 2019, **9**, 1901096.
42 L. Xiao, Y. Cao, J. Xiao, W. Wang, L. Kovarik, Z. Nie and J. Liu, *Chemical Communications*, 2012, **48**, 3321–3323.
43 K.-H. Nam, J.-H. Choi and C.-M. Park, *J. Electrochem. Soc.*, 2017, **164**, A2056.
44 Y. Zhao and A. Manthiram, *Chem. Mater.*, 2015, **27**, 3096–3101.
45 W. P. Kalisvaart, B. C. Olsen, E. J. Luber and J. M. Buriak, *ACS Appl. Energy Mater.*, 2019, **2**, 2205–2213.
46 W. Li, T. Liu, J. Zhang, N. Peng, R. Zheng, H. Yu, Y. Bai, Y. Cui and J. Shu, *Sustainable Energy Fuels*, 2019, **3**, 2668–2674.
47 L. Blondeau, E. Foy, H. Khodja and M. Gauthier, *The Journal of Physical Chemistry C*, 2019, **123**, 1120–1126.
48 H. Usui, Y. Domi, N. Takada and H. Sakaguchi, *Crystal Growth & Design*, 2021, **21**, 218–226.
49 T. Sarakonsri, C. S. Johnson, S. A. Hackney and M. M. Thackeray, *Journal of Power Sources*, 2006, **153**, 319–327.
50 A. P. Hammersley, *J Appl Cryst*, 2016, **49**, 646–652.
51 D. A. Shirley, *Phys. Rev. B*, 1972, **5**, 4709–4714.
52 K. Ersching, C. E. M. Campos, J. C. de Lima and T. A. Grandi, *Materials Chemistry and Physics*, 2008, **112**, 745–748.
53 A. L. Patterson, *Phys. Rev.*, 1939, **56**, 978–982.
54 K. E. Hnida, S. Bäßler, J. Mech, K. Szaciłowski, R. P. Socha, M. Gajewska, K. Nielsch, M. Przybylski and G. D. Sulka, *J. Mater. Chem. C*, 2016, **4**, 1345–1350.
55 L. Bodenes, A. Darwiche, L. Monconduit and H. Martinez, *Journal of Power Sources*, 2015, **273**, 14–24.
56 Y. Zhu, X. Han, Y. Xu, Y. Liu, S. Zheng, K. Xu, L. Hu and C. Wang, *ACS Nano*, 2013, **7**, 6378–6386.
57 A. Darwiche, C. Marino, M. T. Sougrati, B. Fraisse, L. Stievano and L. Monconduit, *J. Am. Chem. Soc.*, 2012, **134**, 20805–20811.
58 S. A. Webb, L. Baggetto, C. A. Bridges and G. M. Veith, *Journal of Power Sources*, 2014, **248**, 1105–1117.
59 S. Komaba, T. Ishikawa, N. Yabuuchi, W. Murata, A. Ito and Y. Ohsawa, *ACS Appl. Mater. Interfaces*, 2011, **3**, 4165–4168.
60 Q. Pan, Y. Wu, F. Zheng, X. Ou, C. Yang, X. Xiong and M. Liu, *Chemical Engineering Journal*, 2018, **348**, 653–660.
61 L. El Ouatani, R. Dedryvère, J.-B. Ledeuil, C. Siret, P. Biensan, J. Desbrières and D. Gonbeau, *Journal of Power Sources*, 2009, **189**, 72–80.

62 J. Vetter, P. Novák, M. R. Wagner, C. Veit, K.-C. Möller, J. O. Besenhard, M. Winter, M. Wohlfahrt-Mehrens, C. Vogler and A. Hammouche, *Journal of Power Sources*, 2005, **147**, 269–281.
63 R. Dedryvère, L. Gireaud, S. Grugeon, S. Laruelle, J.-M. Tarascon and D. Gonbeau, *J. Phys. Chem. B*, 2005, **109**, 15868–15875.
64 M. Moshkovich, Y. Gofer and D. Aurbach, *J. Electrochem. Soc.*, 2001, **148**, E155.
65 L. Baggetto, P. Ganesh, C.-N. Sun, R. A. Meisner, T. A. Zawodzinski and G. M. Veith, *J. Mater. Chem. A*, 2013, **1**, 7985–7994.
66 L. Hu, C. Shang, L. Huang, X. Wang and G. Zhou, *Ionics*, 2020, **26**, 719–726.
67 P. K. Allan, J. M. Griffin, A. Darwiche, O. J. Borkiewicz, K. M. Wiaderek, K. W. Chapman, A. J. Morris, P. J. Chupas, L. Monconduit and C. P. Grey, *J. Am. Chem. Soc.*, 2016, **138**, 2352–2365.
68 S. C. Sevov and J. D. Corbett, *Inorg. Chem.*, 1992, **31**, 1895–1901.

Table of Contents/Abstract graphic

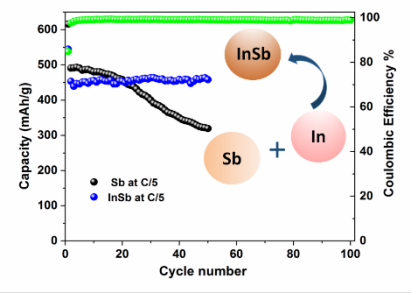

The paper reports the performance of nanostructured InSb alloy as a promising negative electrode for sodium-ion batteries